Capacitor Voltage Ripple Minimization of a Modular Three-Phase AC/DC Power Electronics Transformer With Four-Winding Power Channel

XIAOHUI LI[1], (Graduate Student Member, IEEE), **LINQIAN CHENG**[1], **LIQUN HE**[1], (Member, IEEE), **ZHONGKUI ZHU**[1], **YONG YANG**[1], (Senior Member, IEEE), AND **CHENG WANG**[2], (Member, IEEE)

[1]School of Rail Transportation, Soochow University, Suzhou 215006, China
[2]School of Automation, Nanjing University of Science and Technology, Nanjing 210094, China

Corresponding author: Liqun He (lqhe@suda.edu.cn)

ABSTRACT Power electronic transformer (PET) with modular cascaded structure has become a flexible interface between AC and DC grids. Nonetheless, the notable 2nd-order ripple power introduced from the AC source requires considerable energy storage in the module capacitors, which is likely to degrade the overall power density and increase system cost. In this paper, a power channel based four-winding PET (PC-PET) is proposed to address such an issue. Owing to the phase-crossing power channels, the low-frequency ripples can cancel each other through magnetic flux counteracting. To improve the accuracy of power decoupling, the effect compromised by inconsistent windings is considered. Accordingly, a proportional-resonant (PR) control based power decoupling strategy for PC-PET incorporated with power balance is proposed to decouple the three-phase low-frequency ripple powers, and minimize the voltage ripple in module capacitors. Additionally, the improvement of power density is discussed based on analyses on power losses, capacitor volume and transformer volume. Simulation and experimental results verified the validity of proposed control strategies.

INDEX TERMS PET, power channel, power decoupling, QAB.

I. INTRODUCTION

Power electronic transformer (PET) contributes to intelligent power flow management while providing reduced weight/volume, improved power quality, enhanced reliability and so forth [1]–[3]. It is playing an important role in modern power system as energy routers to replace line-frequency transformer (LFT) [4], [5]. In three-phase AC/DC application, the PET can reduce the required volume and weight to nearly one third, halve the power loss while the material cost can still compete with LFT [6].

The configuration of AC/DC PET can be categorized into two general types: AC/HFAC (high-frequency AC)-HFAC/DC, and AC/DC-DC/HFAC-HFAC/DC. Tough

control issues of matrix converters are hiding the former configuration from high voltage/high power applications. On the contrary, the AC/DC-DC/HFAC-HFAC/DC one is attracting more and more attentions owing to its mature control schemes [1], [7]. Cascaded H-bridge (CHB) and modular multilevel converter (MMC) based PET are both with AC/DC-DC/HFAC-HFAC/DC configuration. Featuring multiport capability and modular structure, these two types of PETs are commonly studied [8]. The MMC-PET [9]–[11] are usually applied when high-voltage DC bus is required. Generally, the topology of a CHB based PET inter-connecting three-phase medium-voltage (MV) AC and low-voltage (LV) DC grid is shown in Fig. 1 with *N* PET modules in each phase. Each module consists of a single-phase PWM rectifier as active front end and a dual-active-bridge (DAB) or multi-active bridge converter [5], [7], [12]. The 2nd-order ripple

powers are introduced from each AC-input-port and stored in DC capacitors of the modules. In order to reduce the 2nd-order ripple in capacitor voltage, large DC capacitance is usually required. This will increase the volume of the system and therefore reduce the power density.
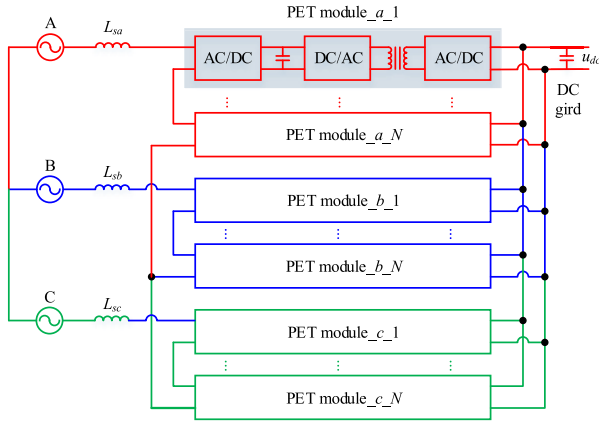

FIGURE 1. The topology of normal three-phase AC/DC CHB-PET.

Power decoupling in single-phase PWM rectifier normally requires large passive capacitors to trap low frequency ripple powers [13]–[17]. As for three-phase systems, interaction between phases makes the ripple powers cancelling each other possible. Quad-active-bridge (QAB) equipped with three primary ports and a secondary port is an ideal way to function as power interaction channels between phases [18], [19]. The power channel based PET (PC-PET) can serve as high-power-density power electronic interface between three-phase three-wire AC and DC grid [20]. However, the three-phase power imbalance issue cannot be ignored. The effect of power decoupling control intensively depends on the collaboration with power balance.

In this paper a proportional-resonant (PR) control based power decoupling strategy for three-phase AC/DC PC-PET is proposed. Realized in stationary reference frame, the strategy provides suppression to multiple harmonics by paralleled controllers. The low-frequency voltage ripples in module capacitors can be minimized even in the situation of asymmetrical three-phase. The capacitance and volume of module capacitor can be reduced, thereby the power density can be improved.

In Section II, the PC-PET configuration is firstly analyzed. Then the 2nd-order ripple voltage in module capacitors and operating principle of PC-PET are discussed. In Section III, the equivalent circuit model of the QAB and its power dispatching characteristics are investigated. In Section IV, the overall control scheme including the proposed ripple voltage suppression strategy is illustrated. In Section V, simulation and experimental results are presented to demonstrate the proposed topology and control schemes. In Section VI, the power losses as well as capacitor volume are calculated based on analytical models. Finally, Section VII concludes this paper.
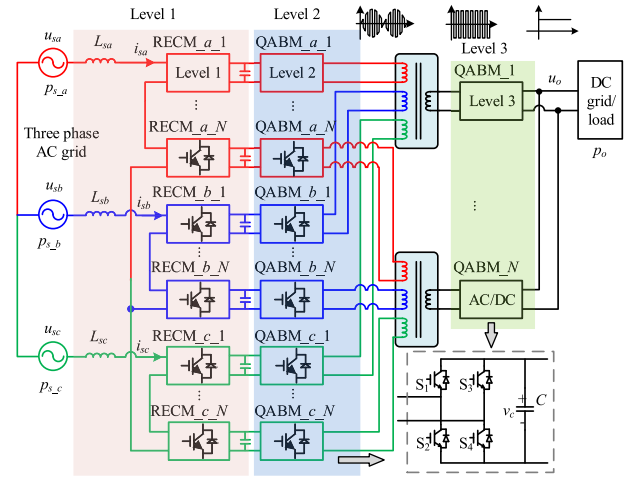

FIGURE 2. The topology of modular PC-PET interfacing three-phase MVAC and LVDC power grids.

II. SECOND-ORDER RIPPLE VOLTAGE ANAYSIS AND OPERATING PRINCIPLE OF PC-PET

The circuit of PC-PET is shown in Fig. 2, with N modules in each phase leg ($a\_1 \sim a\_N$, $b\_1 \sim b\_N$, $c\_1 \sim c\_N$). The PC-PET is composed of three power conversion stages, i.e. level 1, level 2 and level 3 sub-converters. For modular design, the sub-converters from a same stage are identical with each other. The level 1 converter is selected as a H-bridge (HB) that functions as a PWM rectifier (RECM_x_j, $x = a, b$ and c, $j = 1 \sim N$). The level 2 converter (three HBs) and level 3 converter (one HB) act as a QAB. Each QAB is equipped with a four-winding high-frequency transformer with three primary ports and one secondary port. The primary ports are connected to the HFAC-outputs of the three power modules QABM_x_j, corresponding to the jth ($j = 1 \sim N$) module in phase x ($x = a, b$ and c). The secondary port is tied with the HFAC-input of the level 3 converter. The total N DC ports are paralleled to form LVDC-bus.

A. SECOND-ORDER RIPPLE VOLTAGE ANALYSIS
The 2nd-order ripple power imported from the AC port and the induced 2nd-order ripple voltage in DC capacitors are analyzed as follows.

Assume the input voltage and current of phase a are:

$$u_{sa} = U_s \sin(\omega t), \quad (1)$$

$$i_{sa} = I_s \sin(\omega t - \theta). \quad (2)$$

where U_s and I_s are the amplitudes, ω and θ are fundamental angular frequency and power factor angle respectively. Taking RECM_a_j for example, the power flowing to the AC port is expressed as:

$$p_{s\_aj} = \frac{u_{sa} \cdot i_{sa}}{N} = \frac{U_s I_s}{2N} \cos\theta - \frac{U_s I_s}{2N} \cos(2\omega t - \theta). \quad (3)$$

It is supposed that losses of the all the active and passive components can be ignored. The DC component of p_{s_aj} is

directly determined by the DC load.

$$\frac{U_s I_s}{2N} \cos \theta = \frac{p_o}{3N} \qquad (4)$$

where p_o is the power consumed by the load.

If the 2nd-order ripple powers of p_{s_aj} (p_{s2_aj}) are totally absorbed by module capacitors, the instantaneous power of capacitor in RECM_*a_j* is

$$p_{C\_aj} = u_{C\_aj} \cdot i_{C\_aj} = \frac{u_{sa} \cdot i_{sa} - i_{sa} \cdot L_s \frac{di_{sa}}{dt}}{N} - p_{dc}. \quad (5)$$

where u_{C_aj} and i_{C_aj} are the capacitor voltage and capacitor current of RECM_*a_j*, L_s is the line-frequency inductance. p_{dc} is the power transferred to the next conversion stage, which only contains DC component.

$$p_{dc} = \frac{p_o}{3N} \qquad (6)$$

Hence u_{C_aj} mainly contains DC and 2nd-order components, as expressed by:

$$u_{C\_aj} = U_{Cdc\_aj} + u_{C2\_aj}. \qquad (7)$$

Then i_{C_aj} can be rewritten to:

$$i_{C\_aj} = C \cdot \frac{du_{C\_aj}}{dt} = C \cdot \frac{d(U_{Cdc\_aj} + u_{C2\_aj})}{dt}$$
$$= C \cdot \frac{du_{C2\_aj}}{dt}. \qquad (8)$$

where C is the capacitance of RECM.

Substituting (2) - (4) and (6) - (8) to (5), devices (9).

$$(U_{Cdc\_aj} + u_{C2\_aj}) \cdot C \cdot \frac{du_{C2\_aj}}{dt}$$
$$= -\frac{U_s I_s}{2N} \cos(2\omega t - \theta) - \frac{\omega L_s I_s^2}{2N} \sin(2\omega t - 2\theta) \quad (9)$$

Considering zero initial voltage for u_{C2_aj} and integrating both sides of (9) by time, (10) can be derived:

$$\frac{1}{2} C u_{C2\_aj}^2 + C U_{Cdc\_aj} u_{C2\_aj}$$
$$= -\frac{U_s I_s}{4\omega N} \sin(2\omega t - \theta) + \frac{L_s I_s^2}{4N} \cos(2\omega t - 2\theta). \quad (10)$$

Then u_{C2_aj} can be solved from (10), as expressed by (11).

$$u_{C2\_aj} = -U_{Cdc\_aj} + \sqrt{U_{Cdc\_aj}^2 - A \cdot \sin(2\omega t - 2\theta + \psi)} \quad (11)$$

where

$$A = \sqrt{\frac{p_o^2}{9(\omega C N)^2} + \left(\frac{p_o}{3\omega C N \cos \theta} \sin \theta - \frac{4 L_s p_o^2}{18 U_s^2 C N \cos^2 \theta}\right)^2}$$

$$\psi = \arctan\left(\tan \theta - \frac{2\omega L_s p_o}{3 U_s^2 \cos^2 \theta}\right)$$

The relationship between the amplitude of u_{C2_aj} (U_{C2_aj}), C and p_o is shown in Fig. 3. U_{C2_aj} will increase with the increasing of p_o or the decreasing of module capacitance.

Similarly, 2nd-order ripple voltage of module capacitors of phase *b* and phase *c* are expressed as:

$$u_{C2\_bj} = -U_{Cdc\_bj}$$
$$+ \sqrt{U_{Cdc\_bj}^2 - A \cdot \sin(2\omega t - 2\theta + 2\pi/3 + \psi)}, \quad (12)$$

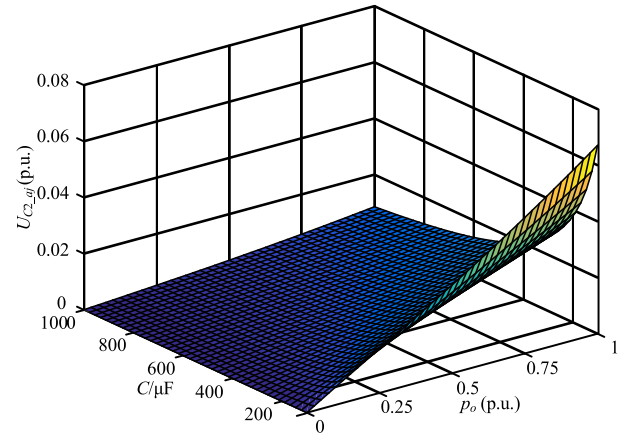**FIGURE 3.** Relationship between amplitude of 2nd-order ripple voltage, *C* and *p_o*.

$$u_{C2\_cj} = -U_{Cdc\_cj}$$
$$+ \sqrt{U_{Cdc\_cj}^2 - A \cdot \sin(2\omega t - 2\theta - 2\pi/3 + \psi)}. \quad (13)$$

B. OPERATING PRINCIPLE OF PC-PET

If the powers flowing through three phases are balanced, the input powers of RECM_*b_j* and RECM_*c_j* are:

$$p_{s\_bj} = \frac{U_s I_s}{2N} \cos \theta - \frac{U_s I_s}{2N} \cos(2\omega t - \theta + 2\pi/3). \quad (14)$$

$$p_{s\_cj} = \frac{U_s I_s}{2N} \cos \theta - \frac{U_s I_s}{2N} \cos(2\omega t - \theta - 2\pi/3). \quad (15)$$

The 2nd-order ripple powers of three phase legs are symmetrical with negative sequence. If the ripple powers are forced to flow through the three primary ports of the four-winding transformer, they will be counteracted through flux coupling. That is the reason why the QAB can be regarded as a "power channel". Only DC component will be reflected on the LVDC bus.

Consequently, there is no low-frequency voltage ripple in all the capacitors of PC-PET. Module capacitors are just required for the purpose of filtering high-frequency switching harmonics. It can sharply reduce the capacitance, the volume as well. In addition, owing to the highly integrated multi-winding structure, the transformer volume is smaller than conventional two-winding ones. All of these make the PC-PET very competitive in terms of power density.

III. EQUIVALENT CIRCUIT MODELING OF THE QAB IN PC-PET

Considering switching frequency components, the controlled voltage source based equivalent circuit of QAB is shown in Fig. 4.

Windings $N_1 \sim N_3$ are the three primary windings of QAB, corresponding to phase $a \sim c$. N_4 is the secondary winding. The inductor L_k ($k = 1 \sim 3$) represents the self-leakage inductance of $N_1 \sim N_3$.

Assuming the phase-shift control (PSC) is employed, the averaged power transferred from port k to port 4 in a
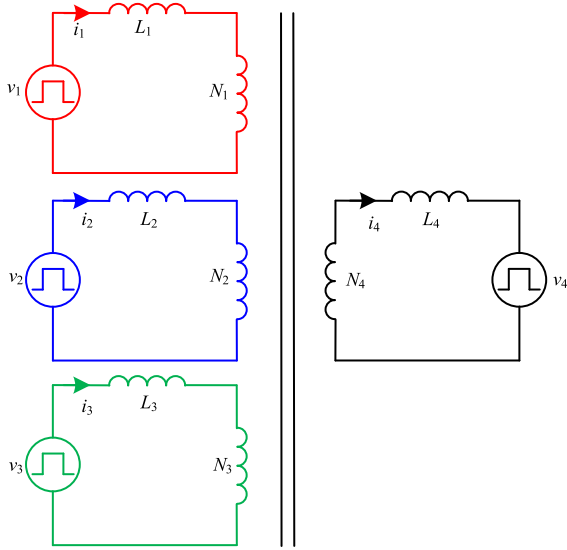
FIGURE 4. Four voltage sources model of four-winding transformer.

switching period can be expressed as [20]:

$$p_{k4} = \frac{1}{T_s} \int_0^{T_s} v_k i(\tau) d\tau = \frac{v_k v_4}{2\pi^2 f_s L_{k4}} \varphi_{k4}(\pi - \varphi_{k4}). \quad (16)$$

where v_k and v_4 are the voltages of port k and port 4, f_s is the switching frequency, T_s is the switching period, L_{k4} is the equivalent inductance between port k and port 4, and φ_{k4} is phase-shift angle between port k and port 4.
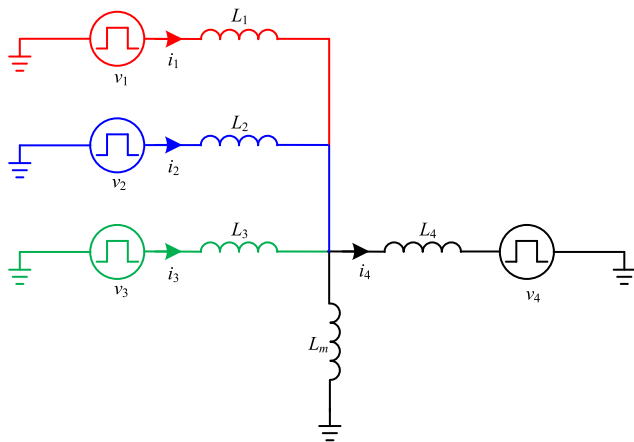

FIGURE 5. T-type equivalent circuit of the four-winding transformer.

According to (16), the power transferred from one primary side to the secondary side is dependent on L_{k4}. It is herein necessary to analysis the value of L_{k4} through an equivalent DAB model. The T type equivalent circuit of four-winding transformer is shown in Fig. 5. L_m is the magnetizing inductance. The Thevenin equivalent circuit between port k and port 4 is given in Fig. 6.
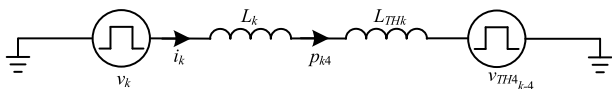

FIGURE 6. Thevenin equivalent circuit between port k and port 4 of QAB.

$v_{TH4_{k-4}}$ is the Thevenin equivalent voltage, that is calculated by

$$\begin{cases} v_{TH4_{1-4}} = \dfrac{L_2 L_3}{L_1 L_3 + L_1 L_2 + L_2 L_3} \cdot v_4 \\ v_{TH4_{2-4}} = \dfrac{L_1 L_3}{L_1 L_2 + L_2 L_3 + L_1 L_3} \cdot v_4 \\ v_{TH4_{3-4}} = \dfrac{L_1 L_2}{L_1 L_3 + L_2 L_3 + L_1 L_2} \cdot v_4. \end{cases} \quad (17)$$

L_{THk} is the Thevenin equivalent leakage inductance and can be calculated by

$$\begin{cases} L_{TH1} = \left(\dfrac{1}{L_m} + \dfrac{1}{L_2} + \dfrac{1}{L_3} + \dfrac{1}{L_4} \right)^{-1} \\ L_{TH2} = \left(\dfrac{1}{L_m} + \dfrac{1}{L_1} + \dfrac{1}{L_3} + \dfrac{1}{L_4} \right)^{-1} \\ L_{TH3} = \left(\dfrac{1}{L_m} + \dfrac{1}{L_1} + \dfrac{1}{L_2} + \dfrac{1}{L_4} \right)^{-1}. \end{cases} \quad (18)$$

Due to the imperfect manufacturing of multi-winding transformer, the leakage inductance of each winding will not be completely consistent. Supposing that the difference value between L_1 and L_2 is ΔL_{12}, and ΔL_{13} is the difference value between L_1 and L_3. The power deviation caused by difference between leakage inductances is addressed. The L_{THk} can then be expressed as:

$$\begin{cases} L_{TH1} = \left(\dfrac{1}{L_m} + \dfrac{1}{L_1 + \Delta L_{12}} + \dfrac{1}{L_1 + \Delta L_{13}} + \dfrac{1}{L_4} \right)^{-1} \\ L_{TH2} = \left(\dfrac{1}{L_m} + \dfrac{1}{L_1} + \dfrac{1}{L_1 + \Delta L_{13}} + \dfrac{1}{L_4} \right)^{-1} \\ L_{TH3} = \left(\dfrac{1}{L_m} + \dfrac{1}{L_1} + \dfrac{1}{L_1 + \Delta L_{12}} + \dfrac{1}{L_4} \right)^{-1}. \end{cases} \quad (19)$$

Power transferred from port k to port 4 can be expressed as:

$$p_{k4} = \frac{v_k v_{TH4_{k-4}}}{2\pi f_s (L_k + L_{THk})} \varphi_{k4}(\pi - \varphi_{k4}). \quad (20)$$

According to (16), (17), (19), (20), L_{k4} can be figured out:

$$\begin{cases} L_{14} = (L_1 + L_{TH1}) \\ \qquad \times \left[L_4 \left(\dfrac{1}{L_m} + \dfrac{1}{L_1 + \Delta L_{12}} + \dfrac{1}{L_1 + \Delta L_{13}} \right) + 1 \right] \\ L_{24} = (L_2 + L_{TH2}) \\ \qquad \times \left[L_4 \left(\dfrac{1}{L_m} + \dfrac{1}{L_1} + \dfrac{1}{L_1 + \Delta L_{13}} \right) + 1 \right] \\ L_{34} = (L_3 + L_{TH3}) \\ \qquad \times \left[L_4 \left(\dfrac{1}{L_m} + \dfrac{1}{L_1} + \dfrac{1}{L_1 + \Delta L_{12}} \right) + 1 \right]. \end{cases} \quad (21)$$

Substituting (21) to (16), taking p_{14} as the base value, the power difference value in per unit is:

$$\begin{cases} \Delta p_{12}(\text{p.u.}) = \dfrac{p_{14} - p_{24}}{p_{14}} = 1 - \dfrac{L_{14}}{L_{24}} \\ \Delta p_{13}(\text{p.u.}) = \dfrac{p_{14} - p_{34}}{p_{14}} = 1 - \dfrac{L_{14}}{L_{34}} \end{cases}. \quad (22)$$
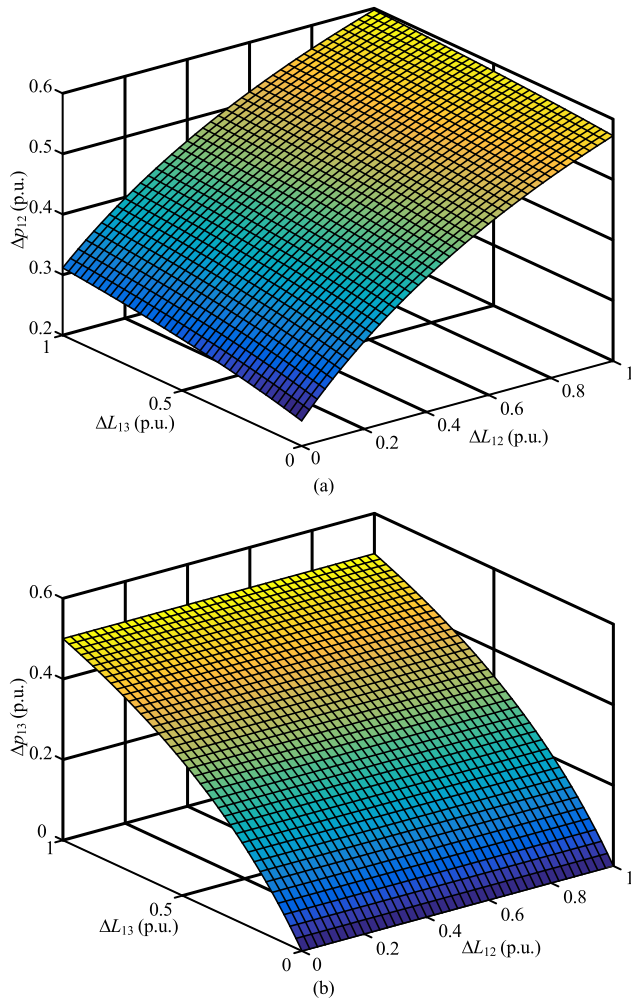
FIGURE 7. The power deviation of QAB with respect to inconsistent leakage inductances of the four-winding transformer: (a) The relationship between Δp_{12}, ΔL_{12} and ΔL_{13}. (b) The relationship between Δp_{13}, ΔL_{12} and ΔL_{13}.

The relationship between ΔL_{12}, ΔL_{13} and Δp_{12} is shown in Fig. 7(a), while the one between ΔL_{12}, ΔL_{13} and Δp_{13} is shown in Fig. 7(b). This shows that a small deviation in leakage inductance can lead to a significant circulating power among different ports of QAB.

Such a power deviation will give rise to three-phase asymmetrical 2nd-order ripple powers and herein pose negative effect on power decoupling of PC-PET. Since such mismatch in transformer windings is inevitable, it is necessary to combine three-phase power balance and power decoupling. The proposed control strategy for PC-PET will be presented in the next section.

IV. PROPOSED CAPACITOR VOLTAGE RIPPLE SUPPRESSION METHOD

The overall control scheme of PC-PET is shown in Fig. 8. The dual-loop control of PWM rectifier is adopted. And the control block diagram for RECM_x_j ($x = a$, b and c, $j = 1 \sim N$) is shown in Fig. 8(a). As the physical constraints

of three-phase system, the voltage regulation of phase c is acquired by the voltage loop of phase a and phase b.

The control block diagram of QAB is shown in Fig. 8(b). The overall control of QAB contains PSC, ripple power decoupling control and power balance control. In the start-up process, the primary HB of QAB works in PWM mode. Duty cycle gradually increases from 0% to 50%, and then switches to PSC.

A. RIPPLE POWER DECOUPLING CONTROL

Besides the 2nd-order component, power stored in module capacitors is likely to have higher secondary induced frequency components, i.e. the 4th-order one. PR control is suitable to decouple multiple-order ripple powers through paralleled structure in stationary reference frames [21]. Here, the PR controller with resonant frequencies of 2ω and 4ω is selected. The transfer function is:

$$PR(s) = k_{RP} + \frac{k_{RI2}s}{s^2 + (2\omega)^2} + \frac{k_{RI4}s}{s^2 + (4\omega)^2}. \quad (23)$$

where k_{RP} is the proportionality coefficient, k_{RI2} and k_{RI4} are the integration coefficients. The resonant part realizes zero-steady-state AC reference tracking, while a proportional gain is employed to ensure fast dynamic response [22]. The block diagram of ripple power decoupling control is shown in Fig.9.

As the physical constraints of three-phase system, Δp_{2_cj} and Δp_{4_cj} can be calculated by:

$$\begin{cases} \Delta p_{2\_cj} = -\Delta p_{2\_aj} - \Delta p_{2\_bj} \\ \Delta p_{4\_cj} = -\Delta p_{4\_aj} - \Delta p_{4\_bj}. \end{cases} \quad (24)$$

According to (3), (14) and (15), the 2nd-order ripple powers (p_{s2_aj}, p_{s2_bj} and p_{s2_cj}) can be calculated as feedforward compensation. The ripple voltages in module capacitors are extracted and suppressed to zero by PR controllers. The p_{r_xj} ($x = a$, b and c) in Fig. 9 can be expressed as:
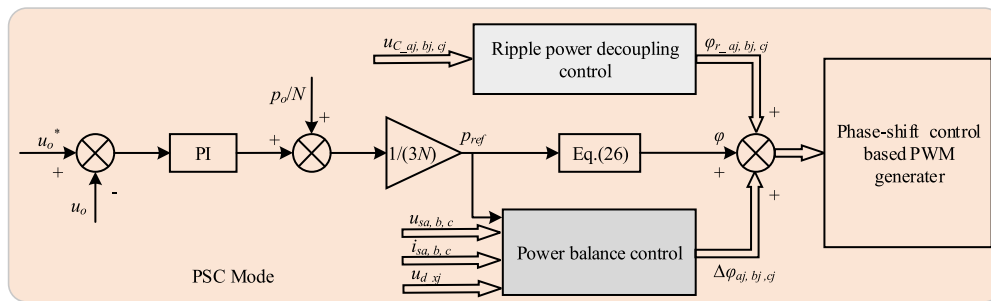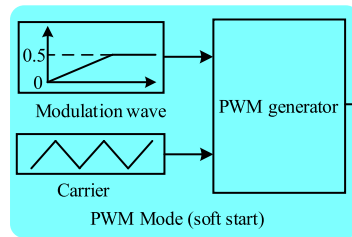
$$\begin{cases} p_{r\_aj} = -\left[\dfrac{U_s I_s}{2N} \cos(2\omega t - \theta) + \Delta p_{2\_aj} + \Delta p_{4\_aj} \right] \\ p_{r\_bj} = -\left[\dfrac{U_s I_s}{2N} \cos(2\omega t - \theta + 2\pi/3) \right. \\ \qquad\qquad \left. + \Delta p_{2\_bj} + \Delta p_{4\_bj} \right] \\ p_{r\_cj} = -\left[\dfrac{U_s I_s}{2N} \cos(2\omega t - \theta - 2\pi/3) \right. \\ \qquad\qquad \left. + \Delta p_{2\_cj} + \Delta p_{4\_cj} \right] \end{cases} \quad (25)$$

According to (16), φ_{r_xj} ($x = a$, b and c) can be expressed as:

$$\begin{cases} \varphi_{r\_aj} = \dfrac{\pi - \pi\sqrt{1 - 8p_{r\_aj}f_s L_{14}/(u_{C\_aj}u_o)}}{2} \\ \varphi_{r\_bj} = \dfrac{\pi - \pi\sqrt{1 - 8p_{r\_bj}f_s L_{24}/(u_{C\_bj}u_o)}}{2} \\ \varphi_{r\_cj} = \dfrac{\pi - \pi\sqrt{1 - 8p_{r\_cj}f_s L_{34}/(u_{C\_cj}u_o)}}{2} \end{cases} \quad (26)$$
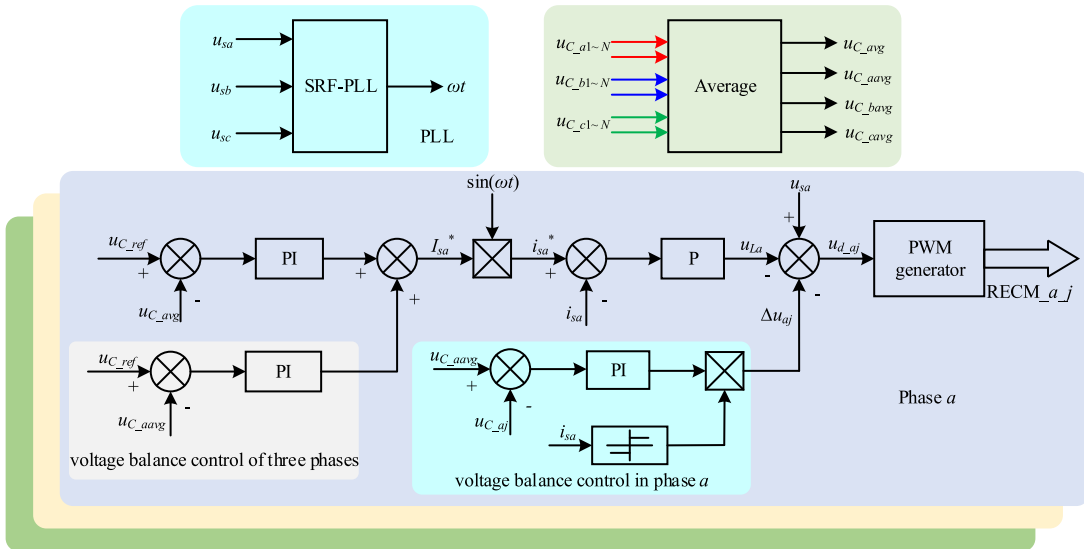
(a)

(b)

FIGURE 8. The control scheme of PC-PET. (a) Control strategy of the PWM rectifiers. (b) Control strategy of QAB involving the whole operating process.
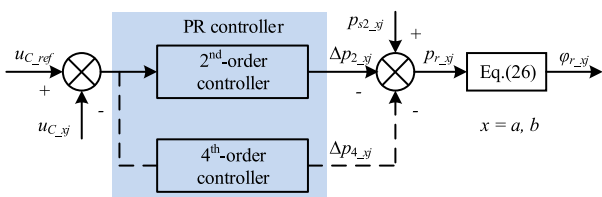

FIGURE 9. The ripple power decoupling control strategy for PC-PET.

B. POWER BALANCE CONTROL

Power imbalance among phases commonly occurs due to inevitable inconsistent circuit parameters, such as different leakage inductance of transformer windings. Consequently, the ripple powers are hard to be completely counteracted, which degrades the effect of ripple power decoupling.

Therefore, a power balance control strategy is introduced. Its control block diagram is shown in Fig. 10.
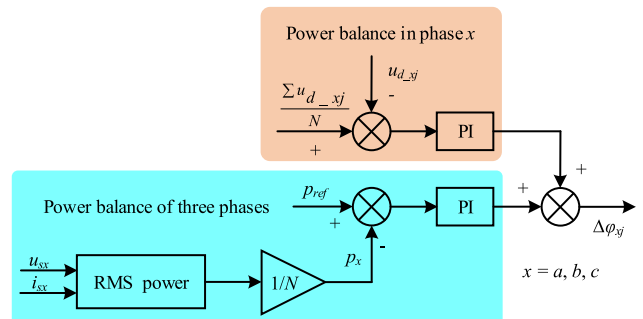

FIGURE 10. The power balance control strategy of QAB in PC-PET.

TABLE 1. Simulation parameters of proposed PC-PET.

Simulation parameters	Value
AC line voltage: V_{ll} (rms)	380 V
Rated power: P	4 kW
No. of module per phase	2
DC-bus voltage: V_{dc}	400 V
Rated voltage of module: V_C	400 V
Switching frequency: f_s	10 kHz
Capacitance in module: C	100 μF
Capacitance at DC bus: C_{dc}	820 μF
Line frequency	50 Hz

TABLE 2. Leakage inductances.

Leakage inductance	Value
Winding 1, phase a: L_{la}	254e^{-6} H
Winding 2, phase b: L_{lb}	264e^{-6} H
Winding 3, phase c: L_{lc}	277.9e^{-6} H

The power balance control strategy is composed of power balance of three phases and power balance in phase x ($x = a$, b and c). According to the power balance control strategy, the compensation on phase-shift angles of QAB ($\Delta\varphi_{aj}$, $\Delta\varphi_{bj}$ and $\Delta\varphi_{cj}$) are finally obtained.

V. SIMULATION AND EXPERIMENTAL VERIFICATION

A. SIMULATION RESULTS AND ANALYSIS

To demonstrate the proposed techniques, a simulation model of PC-PET with two QAB modules per phase is set up in MATLAB/Simulink. Parameters of the power circuit are summarized in Table 1.

To illustrate the influence of inconsistently coiled windings, and to verify the effect of proposed power balancing control, the leakage inductances of the four-winding transformer in QAB are deliberately set as the specific values shown in Table 2. The largest parameter difference is 9.4%.

Fig. 11 and Fig. 12 depict the steady-state as well as dynamic performance of proposed power balancing control for PC-PET. In Fig. 11(a), imbalance percentage of three-phase gird currents caused by inconsistent windings can be as large as 28.3%. While in Fig. 11(b), three-phase grid currents are well balanced. Fig. 12 shows that balancing adjustment is achieved within an interval of 11 periods.

The voltage of module capacitor and its FFT analysis results are shown for comparison in Fig. 13. Without ripple power decoupling, the peak-to-peak of capacitor voltage can be as large as 10%, and the 2nd-order ripple component reaches 5.11% (shown in Fig. 13(a)). With ripple power decoupling applied, the peak-to-peak ratio of the capacitor
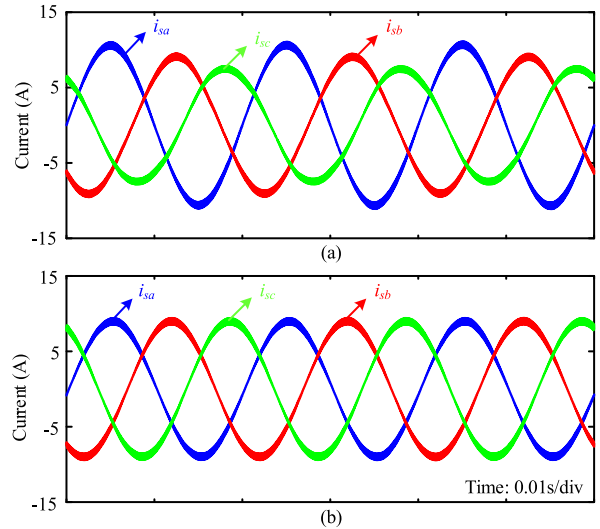

FIGURE 11. Steady-state waveforms of grid-side currents i_{sa}, i_{sb} and i_{sc}. (a) Without power balance control. (b) With power balance control.
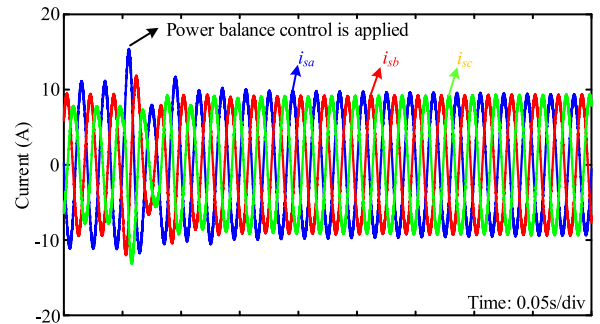

FIGURE 12. Transient waveforms of grid-side currents i_{sa}, i_{sb} and i_{sc} during the starting of power balance control.

voltage is decreased to 0.5%, and the 2nd-order ripple component remains only 0.125% (shown in Fig. 13(b)). The results reveal that the proposed PC-PET control strategy can effectively suppress the voltage ripple in module capacitors.

Fig. 14 shows the primary-side current of four-winding transformer and phase-shift angle of QAB with ripple power decoupling. The 2nd-order component of phase-shift angle contributes to the transfering of 2nd-order ripple power. And the transformer current is high-frequency pulsating with double line-frequency ripple.

The steady-state of PC-PET with the overall control scheme is presented in Fig. 15. As shown, the unit power factor at grid side is always guaranteed. The capacitor voltages and the output voltage of QAB are all well balanced. Through FFT analysis, the THD of gird current is 3.18%, the 2nd-order harmonic component is 0.02%, and other harmonic components are all below 2%.

The effects of power imbalance on ripple power decoupling are shown in Fig. 16. Without power balance control, the three-phase gird currents become asymmetrical as shown in Fig. 16(a). The imbalanced three-phase ripple powers cannot be completely counteracted in power decoupling, leaving
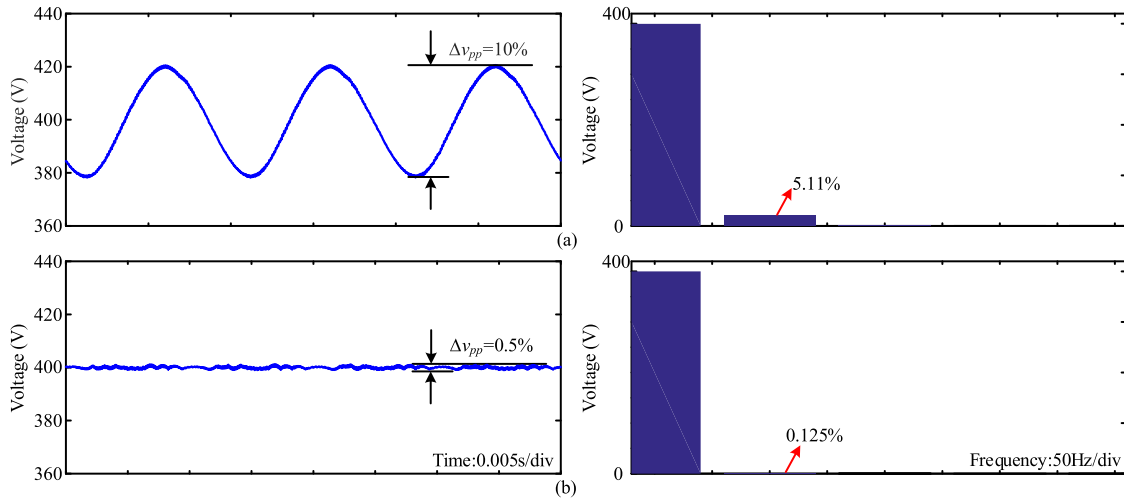
FIGURE 13. Module capacitor voltage u_{C_a1} and the corresponding FFT analysis results. (a) Without ripple power decoupling. (b) With ripple power decoupling.
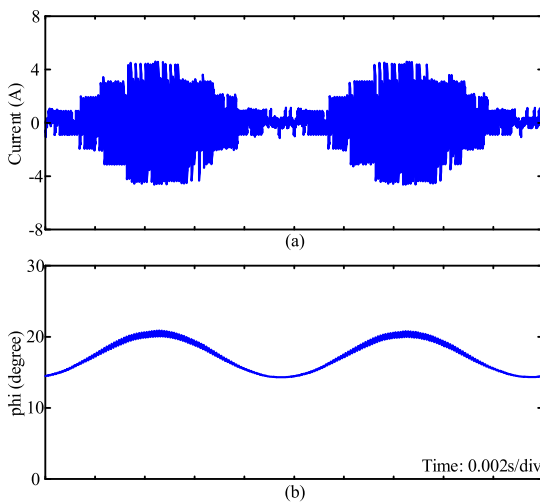

FIGURE 14. Steady-state waveforms with the proposed control scheme. (a) Primary-side current of transformer. (b) Phase-shift angle. (all in phase *a*).

FIGURE 15. Steady-state waveforms with the proposed control scheme. (a) Phase voltage and grid current of phase *a*. (b) Capacitor voltages of power modules in three phases. (c) DC output voltage.

considerable voltage ripple in module capacitor even though power decoupling is applied (shown in Fig. 16(b)). The residual ripple powers are transferred to the secondary side of QAB and lead to low-frequency voltage ripples at the DC bus, as illustrated in Fig. 16(c).

In the same PC-PET without proposed power decoupling, 3000μF capacitance in power modules is required to achieve the effect that the ratio of peak to peak ripple voltage equals to 0.5%. The waveforms of capacitor voltages in both scenarios are shown in Fig. 17. The histogram in Fig. 18 indicates that module capacitance can be sharply reduced by using proposed ripple power decoupling.

Fig. 19 shows the transient processes of PC-PET with 50% load change. It can be seen that with step load changing, the power balance control and ripple power decoupling control can function as expected. During the load change, the system remains operating stably and adjusts to new steady state within 3 fundamental periods.
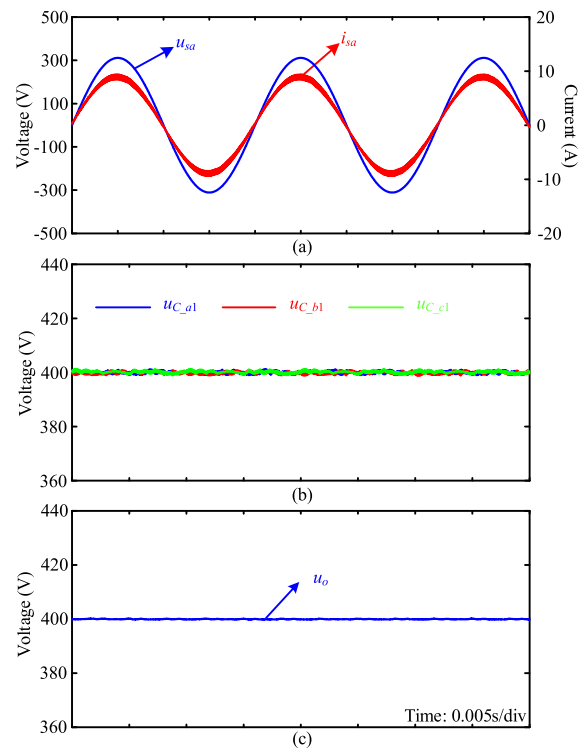
B. EXPERIMENTAL RESULTS AND ANALYSIS

In order to further verify the effectiveness of the proposed control strategy, a 4:1 downscaled PC-PET prototype is built up. Parameters of the prototype is listed in Tabel 3.

Fig. 20 shows of the main control board and the power unit used. The overall setup is shown in Fig. 21. On the main control board, the FPGA (EP1C12Q240I7) receives the modulating signals from the DSP (TMS320F28335) and performs the pulse-width modulation. Based on modular design, the main circuit of PC-PET is constituted by 7 identical power
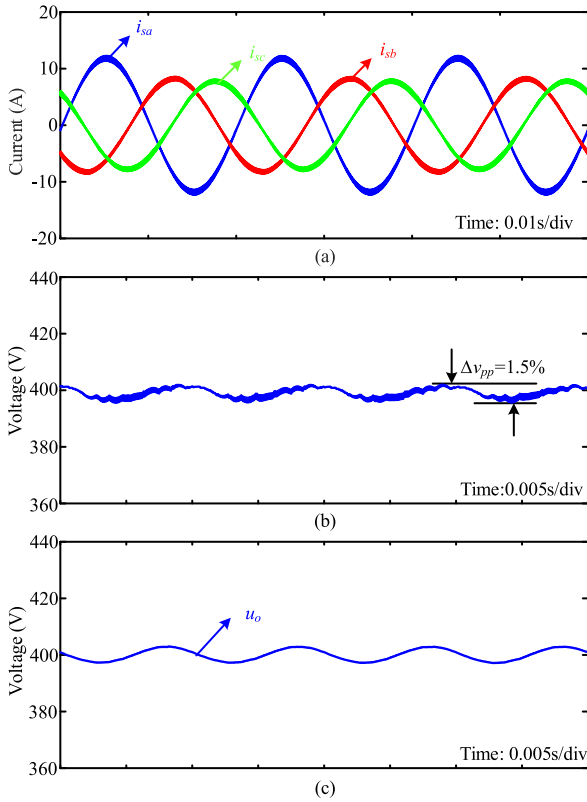
FIGURE 16. Steady-state waveforms of ripple power decoupling without power balance control. (a) Three-phase grid side currents. (b) Module capacitor voltage u_{C_ax1}. (c) DC output voltage of PC-PET.
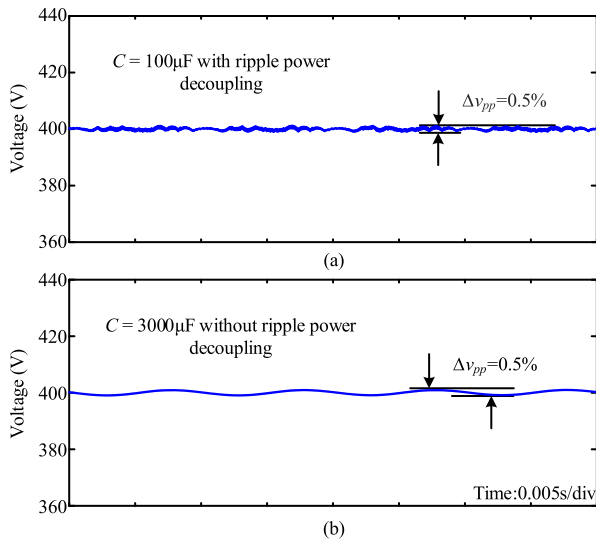

FIGURE 17. The module capacitor voltage. (a) With the proposed power decoupling control/ capacitance of 100μF. (b) Without ripple power decoupling/ capacitance of 3000μF. (all in phase *a*).

FIGURE 18. Capacitance comparison of each individual module.

FIGURE 19. Transient waveforms of PC-PET with 50% load change. (a) Module capacitor voltages. (b) Three-phase grid-side currents. (c) Currents flowing through three primary sides of transformer. (d) Output DC voltage.

units per each cascaded level. The power devices and driving circuit are integrated on one power unit. Each unit has a H-bridge composed of 4 IXFH40N85X MOSFETs (850V/40A), an EP4CE10E22C8 FPGA and other auxiliary circuits. The MOSFETs gating signals are generated by the main control board and transferred to power units by optical fibers.
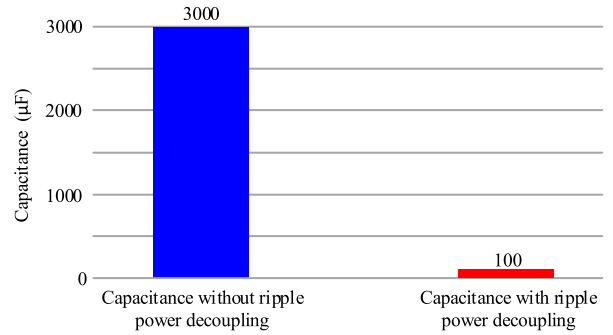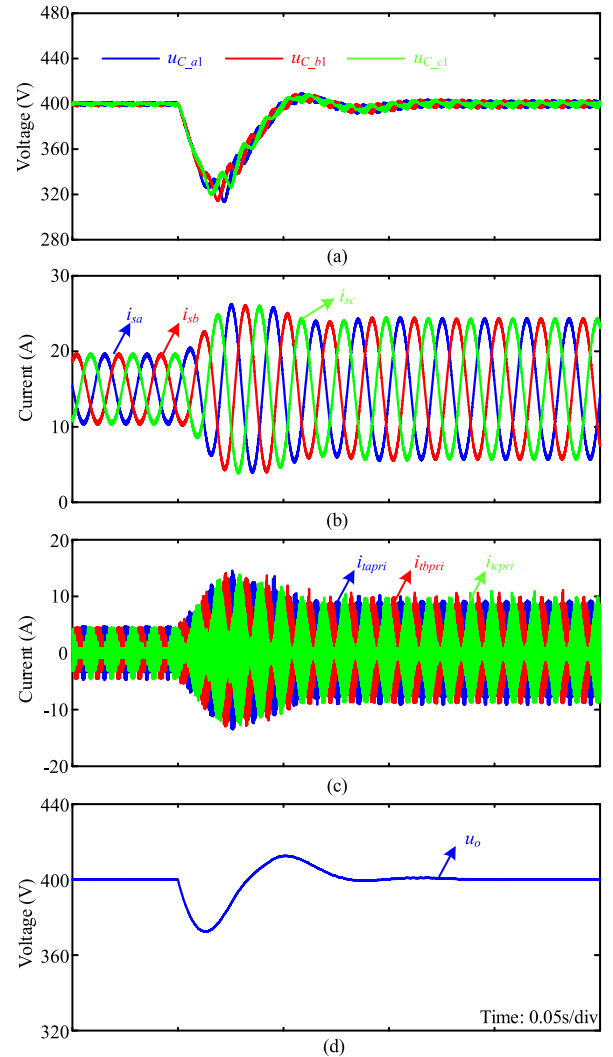
Fig. 22 shows the module capacitor voltages and DC output voltage of PC-PET during the whole operating interval. Firstly, three single-phase PWM rectifiers are working in diode rectifying mode. During the rectifying process, the module capacitor voltages rise from 311V to 400V. Afterwards, the QAB is softly started with a certain ramp rate
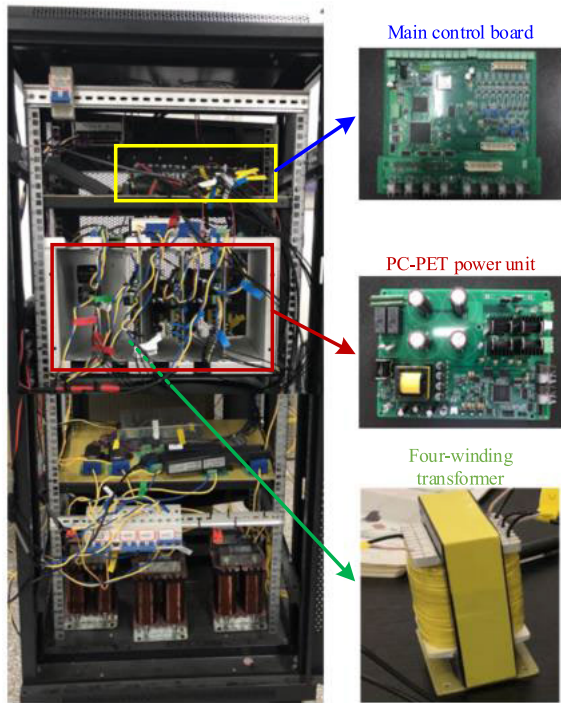
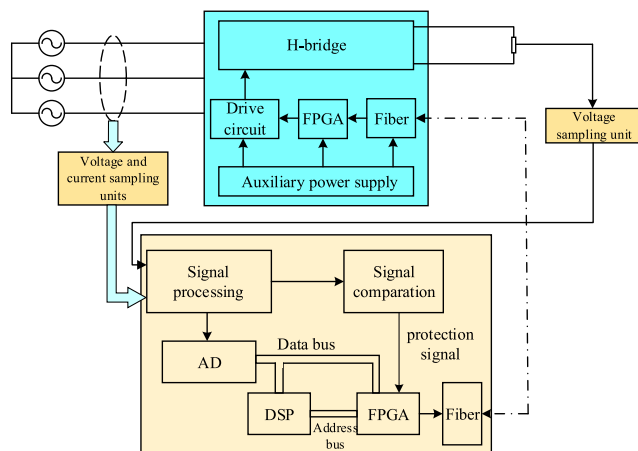**FIGURE 20.** The PC-PET prototype for experimental verification.

FIGURE 21. Schematic diagram of the prototype configuration.
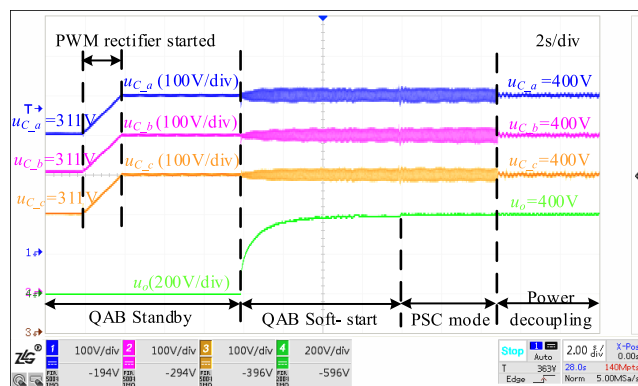

FIGURE 22. Module capacitor voltages and DC output voltage of PC-PET in the whole operating process.

of the pulse width. Once the output voltage reaches 398V, QAB enters PSC operating mode. Finally, the ripple power

decoupling control is imposed. The output voltage of QAB is well regulated and stabilized at the expected value, 400V.
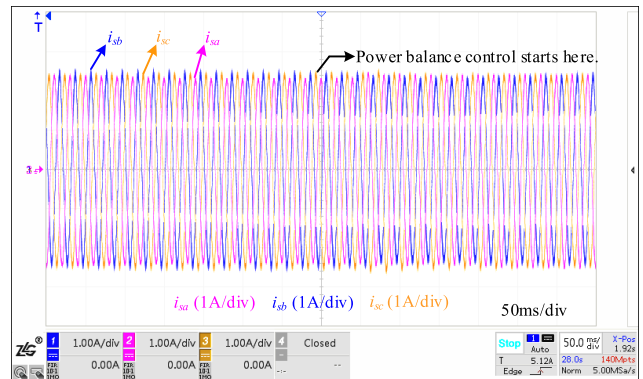

FIGURE 23. Three-phase grid-side currents of PC-PET during the starting of power balance control.

Since the three primary leakage inductances of the four-winding transformer are different, the power balance control should be carried out after entering to the PSC mode. Fig. 23 illustrates the corresponding transient process. When the power balance control is not imposed, imbalance percentage of gird currents can be as large as 11.7%. After when the power balance control effects, the three-phase currents gradually tend to be symmetrical.
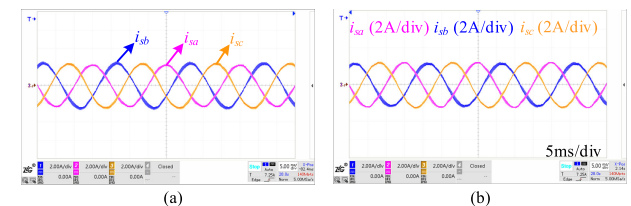

FIGURE 24. Steady-state waveforms of grid-side currents. (a) Without power balance control. (b) With power balance control.

Fig. 24 shows the steady state waveforms of grid side currents with/ without the power balance control. Originally, the three grid currents show considerable amplitude differences due to asymmetrical circuit parameters. Such differences are finally resolved by using the power balance control.

Fig. 25 shows the transient process for ripple power decoupling. As ripple power decoupling control started, the low-frequency ripples in module capacitor voltages are suppressed effectively.

Fig. 26 demonstrates the effect of voltage ripple suppression. Without ripple power decoupling, the peak to peak ratio of ripple voltage is 6.75%. With proposed power decoupling, the peak to peak ratio of ripple voltage is decreased to 1.25%.

The three primary currents of the four-winding transformer with ripple power decoupling are shown in Fig. 27. The waveforms match with simulation results well, and the three primary currents are symmetrical with each other.
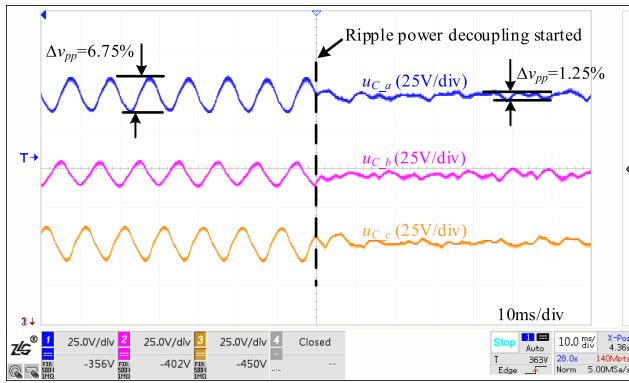
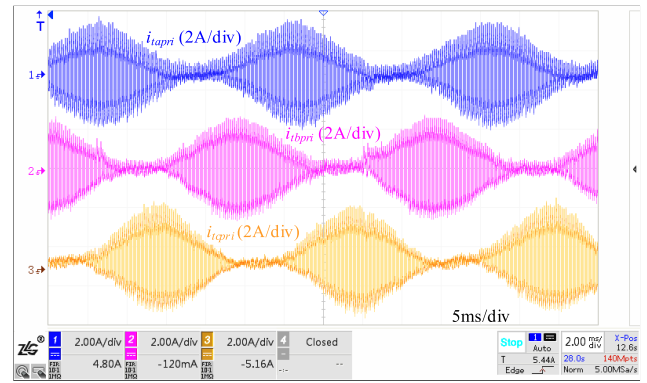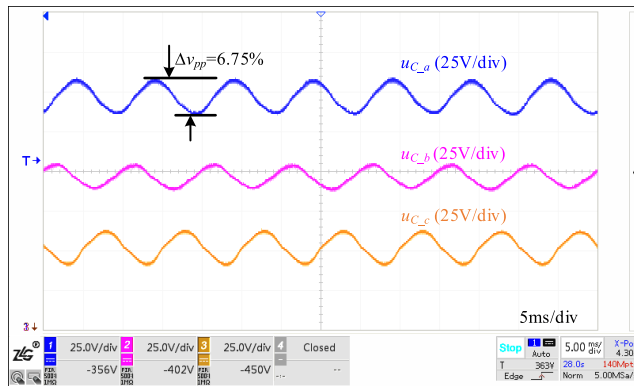**FIGURE 25.** Module capacitor voltages during the starting process of proposed power decoupling control.

(a)

(b)

FIGURE 26. Comparison of module capacitors voltages in PC-PET. (a) Without ripple power decoupling. (b) With proposed ripple power decoupling control.

Fig. 28 shows grid side currents and grid side voltage of phase *a* with ripple power decoupling. Taking phase *a* for example, the current is in phase with the voltage at grid side. Thus, it is proved that ripple power decoupling will not affect the power factor control of PWM rectifier in PC-PET.

Fig. 29 shows the dynamic waveforms of 33% load change, i.e. load power changing from 960W to 1450W. As we shall see, PC-PET can always operate stably. In Fig. 29(a), although there is a transient drop of u_o, such a drop value is only 23V, about 5.75% of the reference value, which is
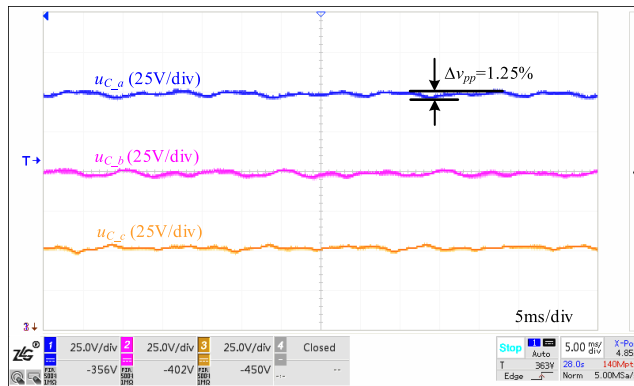

FIGURE 27. Currents flowing through three primary sides of the four-winding transformer in QAB (with proposed power decoupling control).
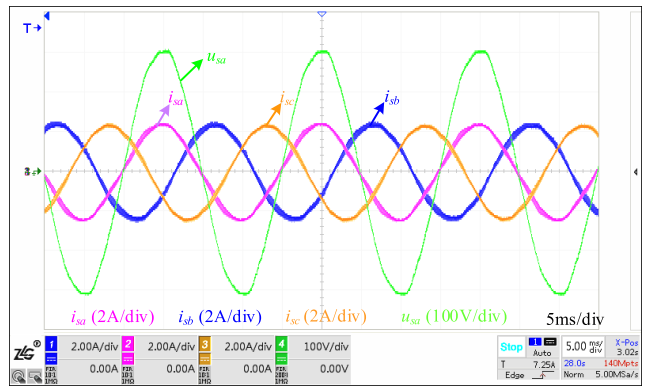
FIGURE 28. Phase *a* voltage and three-phase currents of PC-PET (with the proposed power decoupling control).

acceptable. It is same for the dc voltages. Moreover, there is no double line frequency ripple on each dc voltage, which indicates the decoupling control works well in the transients. In Fig. 29(b), during the load change, the three-phase currents are symmetrical, the power balance control can function well.

VI. POWER LOSSES ANALYSIS

The power dissipation comes from different parts, i.e the semiconductors, the high-frequency transformers, the reactive components. So the power loss calculation are performed from part to part, based on the simulation results.

A. POWER LOSSES IN POWER DEVICES

IGBT power losses can be divided into two groups: conduction loss and switching loss. The conduction loss of IGBT (p_{CT}) and the anti-parallel diode (p_{CD}) can be expressed as [23]:

$$\begin{cases} p_{CT} = \dfrac{1}{T_s} \displaystyle\int_0^{T_s} \left(u_{CE0} \cdot i_C(t) + r_C \cdot i_C^2(t) \right) dt \\ p_{CD} = \dfrac{1}{T_s} \displaystyle\int_0^{T_s} \left(u_{D0} \cdot i_D(t) + r_D \cdot i_D^2(t) \right) dt \end{cases} \quad (27)$$

FIGURE 29. Transient waveforms of PC-PET with 33% load change. (a) Modular capacitor voltages and DC output voltage. (b) Three-phase grid-side currents.

where $i_C(t)$ is the current flowing through collector of IGBT, $i_D(t)$ is the current flowing through the anti-parallel diode. u_{CE0} and r_C repres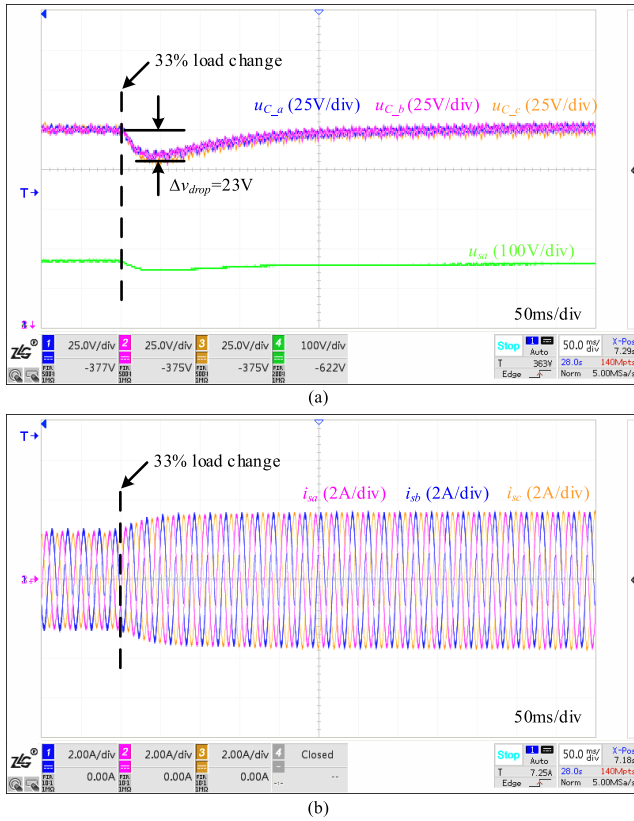ent the on-state voltage the on-state resistance of IGBT respectively, u_{CE0} and r_C represents the on-state voltage the on-state resistance of the anti-parallel diode respectively. u_{CE0}, r_C, u_{D0} and r_D can be calculated referring to datasheet [24]. Switching loss (p_{sw}) can be expressed as:

$$p_{sw} = (E_{onT} + E_{offT} + E_{onD}) \cdot f_s \qquad (28)$$

where E_{onT} and E_{offT} are turn-on and turn-off energy losses in IGBT. E_{onD} is turn-on energy loss in anti-parallel diode. Parameters E_{onT}, E_{offT} and E_{onD} can be found in [24]. The total power losses of an IGBT (p_I) can be calculated with:

$$p_I = p_{CD} + p_{CT} + p_{sw} \qquad (29)$$

B. POWER LOSSES IN FOUR-WINDING TRANSFORMER
Power losses of the four-winding transformer is composed by two parts: core loss and winding loss. Based on the improved Steinmetz equation, the core losses can be calculated as [25],

$$p_C = FKf_s^\alpha B^\beta V \qquad (30)$$

For square excitation, the flux waveform factor F equals to $\pi/4$. The values of K, α and β are 4.88×10^{-5}, 1.63 and 6.22 respectively, corresponding to the ferrite core. B is the flux density, and V is the volume of core.

Neglecting proximity effect and skin effect, the winding loss p_w is calculated by equivalent resistance of the coils. The total power losses (p_T) of four-winding transformer can be calculated by:

$$p_T = p_C + p_W \qquad (31)$$

C. POWER LOSS IN STORAGE CAPACITOR
Power loss of capacitor p_C is mainly consumed by the equivalent series resistance (ESR) that can be calculated as [26]:

$$R_C = \frac{\tan(\delta)}{2\pi f_s C} \qquad (32)$$

where $\tan(\delta)$ is the dissipation factor [27]. Then p_C can be calculated as:

$$p_C = I_C^2 \cdot R_C \qquad (33)$$
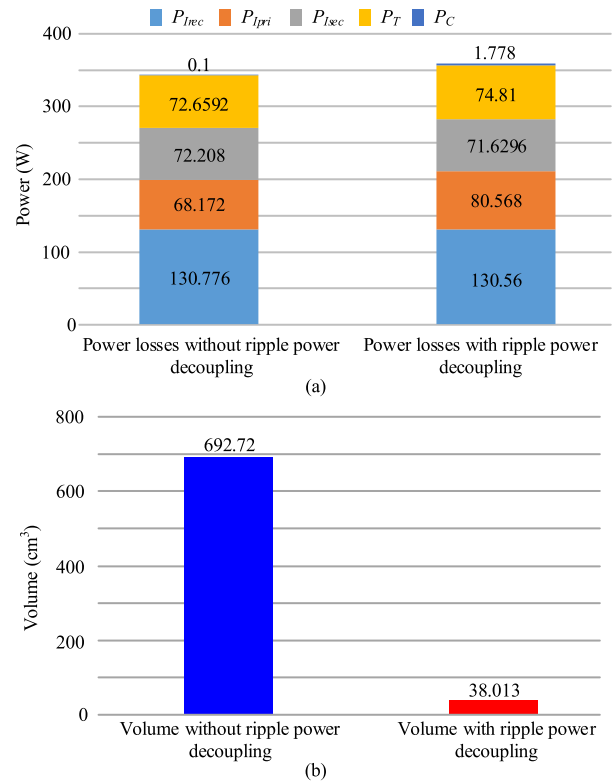
FIGURE 30. Comparisons between PC-PETs with and without the power decoupling. (a) Losses breakdown among components. (b) Total volume of all capacitors.

D. POWER LOSSES AND VOLUME ESTIMATION
Power losses and capacitor volume are calculated based on the selected components listed in Table 4. Similarly, both of the conditions with and without ripple power decoupling are accounted. The comparison results are illustrated in Fig. 30. In Fig. 30(a), P_{Irec}, P_{Ipri} and P_{Isec} represent power loss of IGBTs in RECM, primary and secondary side of QAB, P_T is the total loss of four-winding transformers and P_C is total loss of all capacitors in PC-PET. Without ripple power decoupling, the total power loss of PC-PET is 345.7674W.

TABLE 3. Parameters of proposed PC-PET prototype.

Simulation parameters	Value
AC line voltage: V_{ll}(rms)	380 V
Rated power: P	960W
No. of module per phase: N	1
DC-bus voltage: V_{dc}	400 V
Rated voltage of module: V_C	400 V
Switching frequency: f_s	10 kHz
Capacitance in module: C	100μF
Capacitance at DC bus: C_{dc}	820μF

TABLE 4. Component list of PC-PET with and without ripple power decoupling.

Component	Without ripple power decoupling	With ripple power decoupling
IGBT in RECM	IKA10N65ET6 (650V/25A)	IKA10N65ET6 (650V/25A)
IGBT in primary HB of QAB	IKA08N65F5(650V/10.8A)	IKA08N65F5(650V/10.8A)
IGBT in secondary HB of QAB	IKA15N65H5 (650V/14A)	IKA15N65H5 (650V/14A)
Core of four-winding transformer	EE85/45/31	EE85/45/31
Capacitor in RECM	420MXH100MEFC SN22X25 (100μF/420V) two in series and two in parallel (4)	420MXH1000MEF CSN35X60 (1000uF/420V) two in series and six in parallel (12)
Capacitor at DC bus	420MXH820MEFC SN35X50 (820μF/420V) two in series and two in parallel (4)	420MXH820MEFC SN35X50 (820μF/420V) two in series and two in parallel (4)

While with ripple power decoupling, the total power loss is 359.39W. The efficiency is 95.47% and 95.13% respectively.

As we shall see, the efficiencies of the conditions with and without power decoupling would be very similar. Since the focus of this paper is on minimizing of the capacitor voltage ripples, a comparison is done as following, in order to demonstrate the effect of capacitance reduction.

In Fig. 30(b), the volume of 100μF module capacitor ($V_{100\mu F}$) is 38.013cm^3. The volume of 3000μF module capacitor ($V_{3000\mu F}$) is 692.72cm^3. By using the power decoupling strategy, the volume of module capacitor can be remarkably reduced while the efficiency of the system almost remains the same. Thereby power density of the system is promoted.

For one power module in a conventional three-phase PET, three two-winding transformers are needed. Supposing that the rated power is 2kW, the ferrite core of transformer is
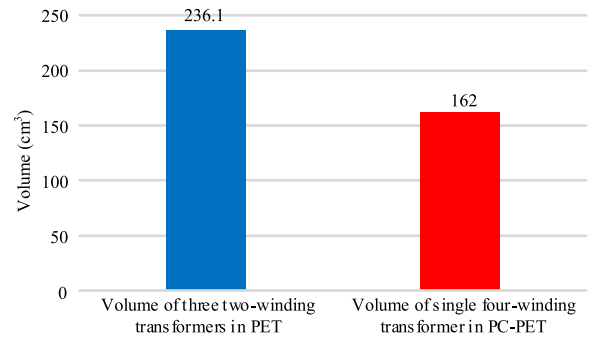

FIGURE 31. Volume comparison of transformers between PET and PC-PET (considering one power module).

EE55/28/25, and the volume is 78.7cm^3. Thus the total volume of transformers in a conventional PET is about 236.1cm^3. For one power module in the proposed PC-PET, only one four-winding transformer is needed. The ferrite core is EE85/45/31, and the total transformer volume in PC-PET is 162cm^3, which is much less than the total one of three two-winding transformers. The comparison of transformer volume between the two types of PET is illustrated in Fig. 31.

VII. CONCLUSION

The low-frequency ripple power in module capacitors prevents PET from promoting its power density. In this paper, a power channel based four-winding PET (PC-PET) is proposed to solve this issue. The PC-PET principle is firstly introduced, which is followed by the mathematical analysis of the ripple power and its induced ripple voltages. Then the negative effect of inconsistent windings on power decoupling is analyzed. Furthermore, the proposed PR control based power decoupling strategy is presented in details. The simulation and experiment results verify that by employing the proposed techniques, the three-phase ripple powers are completely eliminated through power channels without flowing to loads. And the low-frequency ripples voltage in module capacitors are effectively suppressed even with asymmetric circuit parameters, which reduces the required module capacitance sharply. Intentionally, the power losses, the capacitor volume and the transformer volume are estimated based on the simulation data. The results show that PC-PET with the power decoupling control has the similar efficiency with before, but benefits a much higher power density..

REFERENCES

[1] X. She, A. Q. Huang, and R. Burgos, "Review of solid-state transformer technologies and their application in power distribution systems," *IEEE J. Emerg. Sel. Topics Power Electron.*, vol. 1, no. 3, pp. 186–198, Sep. 2013.

[2] J. E. Huber and J. W. Kolar, "Solid-state transformers: On the origins and evolution of key concepts," *IEEE Ind. Electron. Mag.*, vol. 10, no. 3, pp. 19–28, Sep. 2016.

[3] A. Q. Huang, "Medium-voltage solid-state transformer: Technology for a smarter and resilient grid," *IEEE Ind. Electron. Mag.*, vol. 10, no. 3, pp. 29–42, Sep. 2016.

[4] A. Q. Huang, M. L. Crow, G. T. Heydt, J. P. Zheng, and S. J. Dale, "The future renewable electric energy delivery and management (FREEDM) system: The energy Internet," *Proc. IEEE*, vol. 99, no. 1, pp. 133–148, Jan. 2011.

[5] C. Gu, Z. Zheng, L. Xu, K. Wang, and Y. Li, "Modeling and control of a multiport power electronic transformer (PET) for electric traction applications," *IEEE Trans. Power Electron.*, vol. 31, no. 2, pp. 915–927, Feb. 2016.

[6] J. E. Huber and J. W. Kolar, "Volume/weight/cost comparison of a 1MVA 10 kV/400 v solid-state against a conventional low-frequency distribution transformer," in *Proc. IEEE Energy Convers. Congr. Expo. (ECCE)*, Sep. 2014, pp. 4545–4552.

[7] L. F. Costa, G. Buticchi, and M. Liserre, "Quad-active-bridge DC–DC converter as cross-link for medium-voltage modular inverters," *IEEE Trans. Ind. Appl.*, vol. 53, no. 2, pp. 1243–1253, Mar. 2017.

[8] F. Briz, M. Lopez, A. Rodriguez, and M. Arias, "Modular power electronic transformers: Modular multilevel converter versus cascaded H-bridge solutions," *IEEE Ind. Electron. Mag.*, vol. 10, no. 4, pp. 6–19, Dec. 2016.

[9] F. Briz, M. Lopez, A. Zapico, A. Rodriguez, and D. Diaz-Reigosa, "Operation and control of MMCs using cells with power transfer capability," in *Proc. IEEE Appl. Power Electron. Conf. Expo. (APEC)*, Mar. 2015, pp. 980–987.

[10] Z. Li, P. Wang, Z. Chu, H. Zhu, Z. Sun, and Y. Li, "A three-phase 10 kVAC-750 VDC power electronic transformer for smart distribution grid," in *Proc. 15th Eur. Conf. Power Electron. Appl. (EPE)*, Sep. 2013, pp. 1–9.

[11] Y. Liu, A. Escobar-Mejia, C. Farnell, Y. Zhang, J. C. Balda, and H. A. Mantooth, "Modular multilevel converter with high-frequency transformers for interfacing hybrid DC and AC microgrid systems," in *Proc. IEEE 5th Int. Symp. Power Electron. Distrib. Gener. Syst. (PEDG)*, Jun. 2014, pp. 1–6.

[12] B. Zhao, Q. Song, W. Liu, and Y. Sun, "Overview of dual-active-bridge isolated bidirectional DC–DC converter for high-frequency-link power-conversion system," *IEEE Trans. Power Electron.*, vol. 29, no. 8, pp. 4091–4106, Aug. 2014.

[13] R. Wang, F. Wang, D. Boroyevich, R. Burgos, R. Lai, P. Ning, and K. Rajashekara, "A high power density single-phase PWM rectifier with active ripple energy storage," *IEEE Trans. Power Electron.*, vol. 26, no. 5, pp. 1430–1443, May 2011.

[14] H. Li, K. Zhang, and H. Zhao, "DC-link active power filter for high-power single-phase PWM converters," *J. Power Electron.*, vol. 12, no. 3, pp. 458–467, May 2012.

[15] B. Liu, W. Song, J. Ma, X. Feng, and W. Li, "Dynamic performance improvement of single-phase PWM converters with power hysteresis control scheme," *IET Power Electron.*, vol. 11, no. 12, pp. 1894–1902, Oct. 2018.

[16] L. Zhang and X. Ruan, "Control schemes for reducing second harmonic current in two-stage single-phase converter: An overview from DC-bus port-impedance characteristics," *IEEE Trans. Power Electron.*, vol. 34, no. 10, pp. 10341–10358, Oct. 2019.

[17] Y. Xia, J. Roy, and R. Ayyanar, "A capacitance-minimized, doubly grounded transformer less photovoltaic inverter with inherent active-power decoupling," *IEEE Trans. Power Electron.*, vol. 32, no. 7, pp. 5188–5201, Jul. 2017.

[18] P. K. Achanta, B. B. Johnson, G.-S. Seo, and D. Maksimovic, "A multilevel DC to three-phase AC architecture for photovoltaic power plants," *IEEE Trans. Energy Convers.*, vol. 34, no. 1, pp. 181–190, Mar. 2019.

[19] L. He, X. Li, Y. Yang, Y. Yuan, and L. Tong, "Modeling and control of three-phase AC-DC power channel based power electronics transformer (PC-PET) with power decoupling," in *Proc. IEEE Int. Power Electron. Appl. Conf. Expo. (PEAC)*, Nov. 2018, pp. 244–249.

[20] S. Falcones, R. Ayyanar, and X. Mao, "A DC–DC multiport-converter-based solid-state transformer integrating distributed generation and storage," *IEEE Trans. Power Electron.*, vol. 28, no. 5, pp. 2192–2203, May 2013.

[21] S. Li, W. Qi, S.-C. Tan, and S. Y. Hui, "Integration of an active filter and a single-phase AC/DC converter with reduced capacitance requirement and component count," *IEEE Trans. Power Electron.*, vol. 31, no. 6, pp. 4121–4137, Jun. 2016.

[22] Z. Li, Y. Li, P. Wang, H. Zhu, C. Liu, and F. Gao, "Single-loop digital control of high-power 400-hz ground power unit for airplanes," *IEEE Trans. Ind. Electron.*, vol. 57, no. 2, pp. 532–543, Feb. 2010.

[23] D. Graovac and M. Pürschel, "IGBT power losses calculation using the data-sheet parameters," *Infineon Appl. Note*, vol. 1, pp. 1–17, Jan. 2009.

[24] *IGBT Power Losses Calculation Using the Data-Sheet Parameters.* Accessed: 2020. [Online]. Available: http://www.infineon.com

[25] Q. Yue, C. Li, Y. Cao, Y. He, B. Cai, Q. Wu, and B. Zhou, "Comprehensive power losses model for electronic power transformer," *IEEE Access*, vol. 6, pp. 14926–14934, 2018.

[26] B. Chen, P. Wang, Y. Wang, W. Li, F. Han, and S. Zhang, "Comparative analysis and optimization of power loss based on the isolated series/multi resonant three-port bidirectional DC-DC converter," *Energies*, vol. 10, no. 10, pp. 1565–1591, Oct. 2017.

[27] *Rubycon_MXH_Catalog.* Accessed: 2020. [Online]. Available: http://www.rubycon.com

XIAOHUI LI (Graduate Student Member, IEEE) received the M.S. degree in control engineering from the School of Control Engineering, Xijing University, Xi'an, China, in 2016. He is currently pursuing the Ph.D. degree in intelligent transportation science and technology with Soochow University, Suzhou, China.

His current research interests include power electronic transformer and multi physics fields of electrical equipment.

LINQIAN CHENG received the bachelor's degree in engineering from the School of Rail Transportation, Soochow University, Suzhou, China, in 2015, where he is currently pursuing the master's degree in traffic information engineering and control.

His current research interest includes modeling and control of power electronic converter.

LIQUN HE (Member, IEEE) received the B.E. and Ph.D. degrees in electrical engineering from the Huazhong University of Science and Technology (HUST), Wuhan, China, in 2010 and 2015, respectively.

She is currently an Associate Professor with Soochow University, Suzhou, China. Her research interests include fully modular power electronics systems, power electronic transformer, railway electrification, and multi physics fields of electrical equipment.

ZHONGKUI ZHU received the B.S. and M.S. degrees in vehicle engineering from the Hefei University of Technology, Hefei, China, in 1997 and 2002, respectively, and the Ph.D. degree in instrumentation science and technology from the University of Science and Technology of China, Hefei, in 2002.

From 2005 to 2012, he was a Lecturer and an Associate Professor with the School of Mechanical and Electrical Engineering, Soochow University, where he has been a Professor with the School of Rail Transportation, since 2012. He is the author of more than 100 articles. His research interests include system monitoring and diagnostics, signal processing, and vehicle system dynamics and control.

YONG YANG (Senior Member, IEEE) received the B.S. degree in automation from Xiangtan University, Xiangtan, China, in 2003, the M.S. degree in electrical engineering from Guizhou University, Guiyang, China, in 2006, and the Ph.D. degree in electrical engineering from Shanghai University, Shanghai, China, in 2010.

From December 2017 to December 2018, he was a Visiting Scholar with the Center for High Performance Power Electronics (CHPPE), The Ohio State University, Columbus, OH, USA. He is currently an Associate Professor with the School of Rail Transportation, Soochow University. He has coauthored more than 60 journal and conference papers. His current research interests include model predictive control in power electronic converters, distributed energy resource interfacing, and high-performance motor drive control.

CHENG WANG (Member, IEEE) received the B.S. degree in electrical engineering and automation from Southwest Jiaotong University, Chengdu, China, in 2011, and the Ph.D. degree in electrical engineering from the Huazhong University of Science and Technology, Wuhan, China, in 2018.

He was a Research Assistant with the Department of Electrical and Computer Engineering, Lehigh University, Bethlehem, PA, USA, from 2014 to 2018. He joined the Nanjing University of Science and Technology, as an Associate Professor, in 2018. His current research interests include microgrids, high-penetrative grid-interactive photovoltaic systems, MV/HV AC-DC/DC-AC power electronics converter systems, modular multilevel converters, and uninterrupted power systems.

• • •